Available online at www.sciencedirect.com
SCIENCE DIRECT®
Journal of Solid State Chemistry 174 (2003) 87–95
JOURNAL OF SOLID STATE CHEMISTRY
http://elsevier.com/locate/jssc

Neutron powder diffraction study of nuclear and magnetic structures of oxidized and reduced $YBa_2Fe_3O_{8+w}$

P. Karen,[a,*] A. Kjekshus,[a] Q. Huang,[b] V.L. Karen,[c] J.W. Lynn,[b] N. Rosov,[b] I. Natali Sora,[d] and A. Santoro[b]

[a] *Department of Chemistry, University of Oslo, P.O. Box 1033, Blindern, N-0315 Oslo, Norway*
[b] *NIST Center for Neutron Research, National Institute of Standards and Technology, Gaithersburg, MD 20899, USA*
[c] *Ceramics Division, National Institute of Standards and Technology, Gaithersburg, MD 20899, USA*
[d] *Department of Mechanical Engineering, University of Brescia, 25123 Brescia, Italy*

Received 30 September 2002; received in revised form 28 March 2003; accepted 8 April 2003

Abstract

$YBa_2Fe_3O_{8+w}$ has been investigated by neutron powder diffraction as function of temperature and oxygen nonstoichiometry close to the limits of the homogeneity range, $-0.24<w<0.12$. The nonstoichiometry in this triple perovskite is achieved either by accommodation of extra oxygen atoms ($w>0$) in the structural layers of Y, or by creating oxygen vacancies ($w<0$) between the BaO layers in the *ab* plane of the octahedrally coordinated Fe. Moderate amounts of these defects do not alter the long-range crystallographic symmetry, which is best described in space group $P4/mmm$ at all temperatures. However, in the most reduced samples, oxygen vacancies order and the nuclear structure becomes orthorhombic ($Pmmm$), thus showing a mirror-like similarity to the behavior of $YBa_2Cu_3O_{6+w'}$ upon oxidation. The effects of nonstoichiometry on these related crystal structures are discussed in terms of bond-valence sums. The cooperative magnetic structure for all compositions is based on a larger cell related to the nuclear cell by the transformation matrix $(1\bar{1}0/110/002)$, having orthorhombic symmetry when the nuclear structure is tetragonal and monoclinic symmetry when the nuclear structure is orthorhombic. The iron moments are coupled antiferromagnetically in all three directions, the Néel temperature is almost constant as a function of w ($T_N \approx 660$ K), and so is also the low-temperature saturation moment $\mu_{AF} \approx 4.0\mu_B$.

Keywords: Yttrium barium iron oxide; Triple-perovskite-type structure; Oxygen-content control; Neutron powder diffraction

1. Introduction

The study of copper-free compounds with structures similar to that of the 123 superconductor $YBa_2Cu_3O_7$ is important for understanding why copper has such a special role in high-T_c superconductivity. In addition, the structural changes induced by the replacement of copper by other metal atoms may help to identify the factors that favor the formation of the triple-perovskite-type structure, which so efficiently stabilizes the high valence state of copper in planes of square-pyramidally coordinated Cu [1,2].

The $YBa_2Fe_3O_8$ phase [3] is hitherto the only example of an analog of $YBa_2Cu_3O_7$ where Cu is fully replaced by another transition metal, while Y and Ba sites are left intact. The integer oxygen content of the iron compound is 8 atoms per formula unit, owing to the octahedral coordinations of iron atoms replacing the square-planar coordinated copper atoms of $YBa_2Cu_3O_7$.

The complete replacement of Cu by Fe may also clarify certain aspects of the relation between superconductivity and magnetism. Superconductivity in cuprates is achieved upon a progressive doping of an antiferromagnetic (AF) state, which leads to a frustration of the AF arrangement, creation of a spin-glass at low temperatures, and finally to formation of a metallic conductor with a superconducting ground state [4–6]. The existence of the frustrated AF state is considered as a possible reason for the pairing of the electron holes due to spin exchange [7,8]. Covalent models have been suggested [6,9–11] for pairing via spins at the oxygen

*Corresponding author. Fax: +47-22-85-55-65.
E-mail address: pavel.karen@kjemi.uio.no (P. Karen).

0022-4596/03/$ - see front matter © 2003 Elsevier Science (USA). All rights reserved.
doi:10.1016/S0022-4596(03)00180-4

atoms, suggesting the formation of a "ferromagnetic" defect which attracts electron holes at the oxygen linkage to the neighboring Cu atom. Similar effects may occur upon valence changes of Fe in $YBa_2Fe_3O_{8+w}$.

The existence of an Fe analog to $YBa_2Cu_3O_7$ was first signaled in two papers [12,13] which, however, did not recognize appropriately its triple-perovskite-type structure and gave incorrect unit-cell parameters. Later, a multi-phase sample was obtained [14] at 1100°C in N_2, and this was analyzed by X-ray powder diffraction (XPD) and Mössbauer spectroscopy. $YBa_2Fe_3O_{7+w''}$ was identified in the mixture, with the symmetry of space group *Pmmm*. Rietveld refinements of the structure gave a value of $w'' = 0.18$ while a value of $w'' = 0.69$ was obtained from chemical analysis by iodometry. Neglecting the question of the oxygen content, this study indicated that an oxygen-defective $YBa_2Fe_3O_8$ could exist. Single-phase $YBa_2Fe_3O_8$ was synthesized [15] by a prolonged procedure at 950°C and its crystal structure (Fig. 1) was determined [3] from neutron powder diffraction (NPD). Attempts to vary the oxygen content in $YBa_2Fe_3O_8$ [15,16] revealed not only that the oxygen content can be decreased, but also that the structure can tolerate addition of small amounts of extra oxygen (some 0.1 per formula unit). The extra oxygen atoms were structurally located by NPD, on a series of samples where the saturated oxygen content was controlled by a progressive substitution of Ca for Y [17]. Raman spectra of the oxidized and reduced versions of $YBa_2Fe_3O_{8+w}$ were found to differ in details

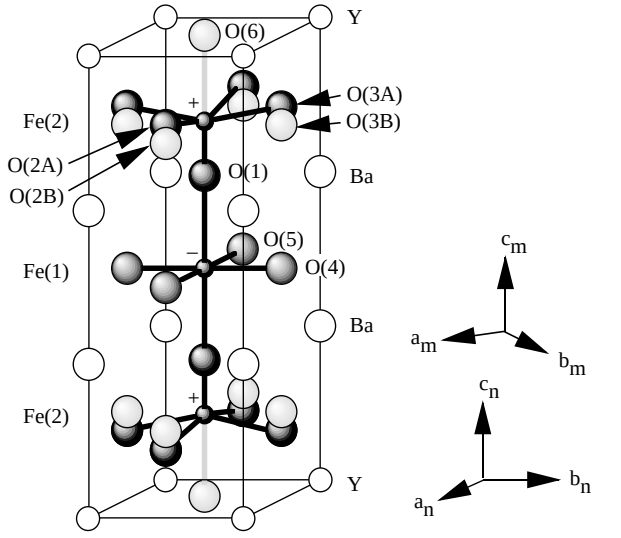

Fig. 1. Schematic representation of nuclear and magnetic structures of $YBa_2Fe_3O_{8+w}$ for both tetragonal and orthorhombic variants. Note that in the tetragonal symmetry O(2A) and O(3A) become equivalent; labeled O(2,3A). The O(2,3B) and O(4,5) labels are derived analogously. Only nuclear cell is represented, with origin at $-\frac{1}{2}, -\frac{1}{2}, -\frac{1}{2}$. The magnetic cell is obtained from the nuclear cell by means of the transformation matrix $(1\bar{1}0/110/002)$. The directions of the magnetic moments of Fe in the G-type structure (marked with + and −) are confined within the *ab* plane.

[18]. The (fine-focus) Raman analyses indicated inter alia that a domain splitting of the oxygen sublattice may take place in samples with the most reduced oxygen content. Another interesting feature which may have its cause in the local structural arrangement is that the AF structure of $YBa_2Fe_3O_{8+w}$, when heated slightly above the Néel temperature, does not revert to the full AF behavior upon cooling [16].

Although the local features may be approached by different methods in future studies, it is very important at this stage to determine reference-quality bulk structural data across the entire (oxygen-content) homogeneity region for $YBa_2Fe_3O_{8+w}$. A long-term equilibration synthesis technique in atmospheres with controlled partial pressures of oxygen was adopted in order to prepare a series of high-quality samples with defined oxygen content. High-resolution NPD data have been used for subsequent Rietveld refinements of the average nuclear and magnetic structures as a function of temperature and oxygen nonstoichiometry.

2. Experimental

2.1. Synthesis

The oxygen saturated master sample, used further for the oxygen content control, was prepared by firing of a precursor obtained from liquid-mixed citrates [19]. Standardized reagent-grade components were used; annealed yttrium oxide (99.99%, Megon), dried barium carbonate (0.8% Sr, Merck) and iron metal, (sheet, 99.99%, Goodfellow Metals). The two former components were dissolved directly in aqueous citric acid (p.a., Fluka), the latter was converted to nitrate by diluted HNO_3 (analyzed, Baker) prior to adding to the hot citrate solution. The citrate solution was evaporated into a viscous melt which was in turn dehydrated at 180°C into a solid xerogel that was milled and incinerated at 450°C in air. The thus obtained amorphous precursor was pressed into tablets and fired four times at 1000°C in a flowing oxygen atmosphere for 100 h with intermittent rehomogenizations.

2.2. Oxygen content control

The equilibrium oxygen content was controlled by varying the partial pressure of oxygen in the reaction atmosphere. Low partial pressures of oxygen were controlled by the high-temperature equilibrium occurring in an argon-based atmosphere (less than 2 ppm O_2 impurity) of hydrogen (5 N purity) and water vapor. The latter was introduced from an ~42.5 wt% solution of H_3PO_4 at room temperature. The partial pressure of $p_{H_2O} \approx 0.02$ atm was corrected for the actual temperature and concentration of H_3PO_4 in the saturator. The

high-temperature composition of the gas was calculated from thermodynamic data [20,21] for H_2O formation. The NPD bulk samples (of cylindrical shape, 15 mm in diameter, 40% porosity, all originating from one batch) were equilibrated at 900°C for 1 week, followed by a relatively rapid cooling (5 min to reach a temperature below 300°C) in the same atmosphere. Elevated pressures of oxygen were applied at 450°C, again with a 1 week equilibration. A 10 atm pressure was obtained in a silica-glass ampoule with Ag_2O and BaO_2, still higher pressures were generated in a silica-glass-lined steel autoclave connected to the oxygen pressure cylinder. In addition, a series of small-scale samples was synthesized for unit-cell parameters and oxygen content measurements.

2.3. Oxygen content analyses

The oxygen content of all samples was determined by titration with Ce(IV) sulfate in acidic solution. When Fe^{II} (and Fe^{III}) was present, the solution of the sample in 3 M HCl was titrated directly, with ferroin as an indicator. When Fe^{IV} (and Fe^{III}) was present, a specified amount of previously titrated Mohr's salt was added and the remaining excess of Fe^{II} was determined. The dissolution of the samples was carried out in glass ampoules sealed in Ar atmosphere. The dissolution time at 100°C was ca. 10 min. The overall iron content in the samples was determined in parallel, after a quantitative reduction of all present iron into Fe^{II} by $SnCl_2$.

2.4. X-ray powder diffraction

The phase purity and unit-cell parameters were evaluated, with the help of the SCANPI package of programs [22], from XPD data obtained using a Guinier–Hägg camera with Cu $K\alpha_1$ radiation and Si as an internal standard. The relative content of additional phases was estimated [23] from observed and calculated intensities for one or several reflections.

2.5. Neutron powder diffraction

The NPD measurements were made at temperatures between 10 and 653 K on the BT-1 high-resolution five-counter diffractometer at the Reactor of the National Institute of Standards and Technology, using the experimental conditions specified in Table 1. All refinements were carried out using the Rietveld method [24] adapted to the multicounter diffractometer arrangements using the GSAS program of Larson and Von Dreele [25].

Table 1
Collection of NPD data

Monochromatic beam:	220 reflection form a Cu crystal
Wavelength:	1.5391(10) Å
Horizontal divergences:	10′–20′–10′ of arc of the in-pile monochromatic beam and diffracted beam collimators, respectively
Sample container:	Vanadium or aluminum can
2θ angular range:	5–120°; steps: 0.05°
Scattering amplitudes:	b(Y) = 775, b(Ba) = 525, b(Fe) = 954, b(O) = 581 fm

Table 2
Characterization of $YBa_2Fe_3O_{8+w}$ bulk samples and conditions of their synthesis

$8+w$	a (Å)	b (Å)	c (Å)	$\log p_{O_2}$ (bar)	t (°C)
8.12(1)	3.9158(8)		11.809(3)	2.2	450
8.11(1)	3.9163(4)		11.808(2)	1.0	450
8.08(1)	3.9151(2)		11.814(1)	0.0	900
7.94(1)	3.9174(3)		11.814(1)	−16.1	900
7.86(1)	3.9200(5)		11.801(4)	−21.5	800
7.76(1)	3.9098(4)	3.9276(4)	11.778(2)	−19.1	900

Note: Oxygen contents by titration, unit-cell parameters by XPD.

3. Results

3.1. Syntheses and characterizations

The products were practically phase-pure $YBa_2Fe_3O_{8+w}$. XPD revealed the presence of ~1 wt% of $(Ba_{1-y}Y_y)FeO_{\sim 3}$. This cubic perovskite occurs in close vicinity to the main phase in the phase diagram [15], and therefore easily appears as the consequence of minor impurities in the reagent-grade starting materials. The XPD unit-cell data and the titration determined oxygen contents for the obtained bulk samples are listed in Table 2 together with the equilibration conditions. By careful adjustments of the hydrogen and water content in the annealing atmosphere, the lower homogeneity limit of $YBa_2Fe_3O_{8+w}$ with respect to oxygen was determined as $w \approx -0.25$ at 900°C. Upon further reduction, a yellow–green Fe^{II} phase appears as the first decomposition product. The upper homogeneity limit with respect to oxygen content has not been crossed in our O_2-pressure equilibrations.

Whereas the stoichiometric parent phase $YBa_2Fe_3O_8$ is tetragonal [3], XPD detects orthorhombic symmetry for compositions accommodating more than some 0.15 oxygen vacancies per formula. Fig. 2 illustrates the relationship between this transition and that occurring upon insertion of oxygens into $YBa_2Cu_3O_6$ [1,2]. In both $YBa_2Fe_3O_8$ and $YBa_2Cu_3O_6$, the local orthorhombic strains due to oxygen defects are random at first, but above certain amounts they prefer long-range ordered arrangements. This is manifested by the onset of

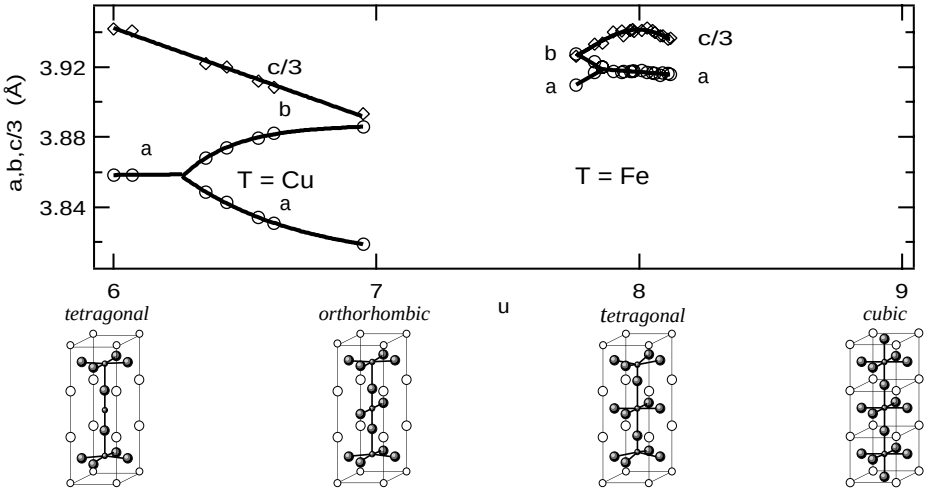

Fig. 2. XPD unit-cell data as functions of oxygen content and T-coordination in triple-perovskite structures; $YBa_2T_3O_u$ with T = Cu (Ref. [2]) and T = Fe (present data). In the structure illustrations, Cu and Fe are shown as small shaded spheres, O as larger shaded spheres, and Ba and Y as open circles of appropriate size.

the orthorhombic distortion of the unit cell. In both structures, the continuous introduction of local orthorhombic strains is also accompanied by a steady contraction of the unit-cell parameter c and a decrease in the unit-cell volume. Because the copper atoms in $YBa_2Cu_3O_6$ also are oxidized in this process, the contraction in the c-axis and unit-cell volume could easily be grasped as a result of the diminishing ionic size of copper. Such an explanation cannot hold for $YBa_2Fe_3O_8$, where iron is reduced and consequently increases its size in parallel with the introduction of the local orthorhombic strains due to the oxygen vacancies.

3.2. Neutron powder diffraction

Structural refinements for $YBa_2Fe_3O_{8+w}$ samples with $w = -0.24$ and -0.14 (w by titration) were carried out in the space group $Pmmm$, for other samples the unit-cell parameter a was constrained to be equal to b, and the atomic coordinates were constrained to obey the symmetry of the space group $P4/mmm$ using as initial parameters those obtained in the previous analyses reported in Refs. [3,17]. The labeling of the sites (Fig. 1) is compatible with both symmetries. The refinement results are summarized according to symmetry in Tables 3 and 4. For typical illustrations of observed and calculated patterns see Refs. [3,17]. Refinements of $YBa_2Fe_3O_{8+w}$ for compositions with $w>0$ were carried out assuming the same location of the added oxygen atoms O(6) as determined previously [17] in the system $(Y_{1-x}Ca_x)Ba_2Fe_3O_{8+w}$. In order to refine the occupancy of O(6), the involved thermal displacement factor was kept fixed at a reasonable value. The values of the occupancies thus obtained were in agreement with the chemical analysis data, within 2σ of the latter determinations. The introduction of the O(6) atoms into the structural model improved all R factors pertinent to the Rietveld refinement. As illustrated in Fig. 1, the structural disorder caused by the accommodation of the large oxygen atoms in the Y layer was modeled by assuming split positions for the fraction of the neighboring O(2,3) atoms corresponding to the amount of the extra oxygens per cell (as done also in Ref. [17]).

For the most reduced samples, still within the homogeneity region, the orthorhombic distortion can be unequivocally established from the splitting of numerous peaks in the powder pattern. Already for the $w = -0.14(1)$ bulk sample, a splitting of the tetragonal reflection 400 into 400 and 040 is seen in the NPD patterns (note: outside the angular range for the Guinier–Hägg XPD technique). The refinements of the nuclear structure for the two most reduced samples were carried out using only the NPD data in the high 2θ range. An additional benefit of this approach was that strong magnetic reflections, which occur at $2\theta<60°$, were avoided. These calculations, in which the occupancies of all the oxygen atoms were varied together with the atomic and profile parameters, showed immediately that the oxygen elimination generates vacancies only in the plane of Fe(1), sandwiched between the two Ba layers. The vacancies are almost exclusively located at the O(4) site, i.e., ordered along the longer orthorhombic axis (b). Interestingly, this is opposite to the situation in $YBa_2Cu_3O_7$, where the fully vacant sites run along the shorter axis (a) and the copper–oxygen squares along b [1,26]. As illustrated in Fig. 2, the range with orthorhombic symmetry for $YBa_2Fe_3O_{8+w}$ is narrow, and this makes it hard to establish the precise onset of this composition-induced, long-range ordering of the oxygen vacancies. On the basis of the standard deviations in the oxygen content determinations and the variation in the occupancy

Table 3
Refined structural parameters of tetragonal $YBa_2Fe_3O_{8+w}$ at 298 K

Titrated w				0.12(1)	0.11(1)	0.08(1)	−0.06(1)
Nuclear unit cell			S.G.	*P4/mmm*	*P4/mmm*	*P4/mmm*	*P4/mmm*
			a (Å)	3.9131(1)	3.9136(1)	3.91300(6)	3.91486(6)
			c (Å)	11.8072(2)	11.8099(2)	11.8128(3)	11.8198(3)
			V (Å^3)	180.79(1)	180.89(2)	180.87(1)	181.15(1)
Y	1*d*	$\frac{1}{2},\frac{1}{2},\frac{1}{2}$	B(Å^2)	0.91(4)	0.79(5)	0.75(4)	0.55(3)
Ba	2*h*	$\frac{1}{2},\frac{1}{2},z$	z	0.1662(2)	0.1664(2)	0.1659(2)	0.1641(2)
			B(Å^2)	0.69(4)	0.78(4)	0.57(4)	0.63(4)
Fe(1)	1*a*	0, 0, 0	B(Å^2)	0.49(3)	0.51(4)	0.44(3)	0.51(3)
Fe(2)	2*g*	0, 0, z	z	0.3397(1)	0.3398(1)	0.3396(1)	0.3398(1)
			B(Å^2)	0.54(2)	0.50(2)	0.45(2)	0.45(2)
O(1)	2*g*	0, 0, z	z	0.1824(2)	0.1818(2)	0.1800(2)	0.1836(2)
			B(Å^2)	1.05(4)	1.02(5)	0.88(4)	0.84(4)
O(2,3A)	4*i*	0, $\frac{1}{2}$, z	z	0.3820(1)	0.3817(1)	0.3818(2)	0.3824(1)
			B(Å^2)	0.53(3)	0.58(3)	0.51(3)	0.60(2)
			n	3.62(1)	3.68(2)	3.76(2)	4.00
O(2,3B)	4*i*	0, $\frac{1}{2}$, z	z	0.3398(2)	0.3394(1)	0.3396(1)	—
			B(Å^2)	0.53(3)	0.58(3)	0.51(3)	—
			n	0.38(1)	0.32(2)	0.24(2)	—
O(4,5)	2*f*	0, $\frac{1}{2}$, 0	B(Å^2)	0.83(3)	0.82(4)	0.65(3)	0.47(5)
			n	2.00	2.00	2.00	1.92(2)
O(6)	1*b*	0, 0, $\frac{1}{2}$	B(Å^2)	1.75	1.75	0.80	—
			n	0.095(3)	0.079(4)	0.059(5)	—
Refined w				0.095(3)	0.079(4)	0.059(5)	−0.08(2)
Magnetic unit cell			S.G.	*Imm′m*	*Imm′m*	*Imm′m*	*Imm′m*
			a (Å)	5.5339(1)	5.5347(1)	5.53382(9)	5.53645(9)
			b (Å)	5.5339(1)	5.5347(1)	5.53382(9)	5.53645(9)
			c (Å)	23.6143(4)	23.6198(4)	23.6256(5)	23.6397(5)
			V (Å^3)	723.17(2)	723.55(3)	724.06(4)	724.61(4)
			μ_{AF}[a] (μ_B)	3.53(2)	3.59(2)	3.48(2)	3.60(2)
χ				1.34	1.27	1.23	1.41
R_p (%)				4.45	4.91	5.79	6.16
R_{wp} (%)				6.01	6.63	7.48	7.60

[a] $\mu_{AF} = \mu_x$; μ_y and μ_z fixed at zero.

factors, it is estimated that the onset of the tetragonal-to-orthorhombic conversion occurs around some $w = -0.15(5)$, as depicted for the XPD-based data in Fig. 2. A symmetry change at $w = -0.15$ is also observed for the isostructural phases $DyBa_2Fe_3O_{8+w}$ and $ErBa_2Fe_3O_{8+w}$ [27].

Inspection of the refined data at different temperatures revealed smooth variations of the nuclear (and magnetic) structure parameters over the entire range of temperatures. As an example, the temperature variations of the unit-cell parameters for tetragonal $YBa_2Fe_3O_{8.08}$ are illustrated in Fig. 3. The thermal expansion of tetragonal $YBa_2Fe_3O_{8.08}$ is of a nonlinear and anisotropic character, but can successfully be fitted by a quadratic function $j(T) = j_0(1 + \alpha_j T + \beta_j T^2)$ with $a_0 = 3.9102(3)$, $c_0 = 11.7900(15)$ Å; $\alpha_a = 1.5(5) \times 10^{-6}$ K^{-1}, $\alpha_c = 4.60(8) \times 10^{-6}$ K^{-1}; $\beta_a = 1.33(7) \times 10^{-8}$ K^{-2}, $\beta_c = 1.84(11) \times 10^{-8}$ K^{-2}. The expansion along c is 2.5 times larger than that of a. The variations in the unit-cell parameters for the most reduced orthorhombic $YBa_2Fe_3O_{7.76}$ sample reveal what may be considered as the beginning of a thermally induced, order–disorder transition at the highest temperatures of the measured range 10–650 K. This behavior is similar to that of $YBa_2Cu_3O_{6+w'}$ in its orthorhombic region.

The inspection of all NPD patterns for $YBa_2Fe_3O_{8+w}$ revealed that magnetic intensities could be accounted for by the same antiferromagnetic model reported previously for the stoichiometric phase [17]. The final results were obtained in each case from refinements in which the atomic, magnetic, and profile parameters were varied simultaneously (Tables 3 and 4). Practically no variation in the ordered magnetic moment μ_{AF} is seen as function of the composition parameter w. As expected, the intensities of the magnetic reflections, and hence the values of the *ordered* magnetic moments of iron decrease as the temperature increases. The decrease in the relative

Table 4
Refined structural parameters of orthorhombic $YBa_2Fe_3O_{8+w}$ at 298 and 10 K

Temperature:				298 K		10 K	
Titrated w				−0.14(1)	−0.24(1)	−0.14(1)	−0.24(1)
Nuclear unit cell			S.G.	*Pmmm*	*Pmmm*	*Pmmm*	*Pmmm*
			a (Å)	3.91095(8)	3.90735(7)	3.90439(8)	3.90027(7)
			b (Å)	3.92223(8)	3.92532(7)	3.91811(8)	3.92095(6)
			c (Å)	11.7916(3)	11.7869(3)	11.7539(4)	11.7494(3)
			V (Å^3)	180.88(1)	180.79(1)	179.81(1)	179.69(1)
Y	1*h*	$\frac{1}{2},\frac{1}{2},\frac{1}{2}$	B(Å^2)	0.55(4)	0.50(3)	0.10(4)	0.13(3)
Ba	2*t*	$\frac{1}{2},\frac{1}{2},z$	z	0.1654(3)	0.1692(2)	0.1654(2)	0.1678(2)
			B(Å^2)	0.63(4)	0.66(3)	0.28(4)	0.24(3)
Fe(1)	1*a*	0, 0, 0	B(Å^2)	0.30(1)	0.52(4)	0.16(4)	0.20(5)
Fe(2)	2*q*	0, 0, z	z	0.3394(1)	0.3399(1)	0.3392(1)	0.3395(1)
			B(Å^2)	0.49(2)	0.46(2)	0.26(2)	0.24(2)
O(1)	2*q*	0, 0, z	z	0.1821(3)	0.1810(2)	0.1817(3)	0.1847(2)
			B(Å^2)	0.68(4)	0.63(4)	0.36(4)	0.48(4)
O(2)	2*s*	$\frac{1}{2}$, 0, z	z	0.3831(7)	0.3834(8)	0.3827(6)	0.3830(4)
			B(Å^2)	0.65(3)	0.57(2)	0.27(3)	0.32(2)
O(3)	2*r*	0, $\frac{1}{2}$, z	z	0.3817(7)	0.3807(4)	0.3814(6)	0.3816(4)
			B(Å^2)	0.65(3)	0.57(2)	0.27(3)	0.32(2)
O(4)	1*e*	0,$\frac{1}{2}$, 0	B(Å^2)	0.55(6)	0.65	0.43(6)	0.40(5)
			n	0.85(3)	0.84(2)	0.86(3)	0.83(2)
O(5)	1*b*	$\frac{1}{2}$, 0, 0	B(Å^2)	0.55(6)	0.65(3)	0.43(6)	0.40(5)
			n	0.99(3)	0.98(2)	0.98(3)	0.96(2)
Refined w				−0.16(4)	−0.18(3)	−0.16(4)	−0.21(3)
Magnetic unit cell			S.G.	$P2'/m$	$P2'/m$	$P2'/m$	$P2'/m$
			a (Å)	5.5389(1)	5.53855(10)	5.5314(1)	5.53046(9)
			b (Å)	5.5389(1)	5.53855(10)	5.5314(1)	5.53046(9)
			c (Å)	23.5832(7)	23.5738(5)	23.5078(7)	23.4989(6)
			γ(°)	90.165(2)	90.263(1)	90.201(2)	90.303(1)
			V (Å^3)	723.52(5)	723.13(4)	719.25(5)	718.72(4)
			μ_{AF}[a] (μ_B)	3.53	3.50(2)	3.80(2)	3.88(2)
χ				1.33	1.34	1.39	1.41
R_p (%)				6.50	5.27	6.82	5.44
R_{wp} (%)				8.19	6.67	8.71	7.02

[a] $\mu_{AF} = \mu_x$; μ_y and μ_z fixed at zero.

spontaneous sublattice magnetization σ can be described by the Brillouin function $B(J,\zeta)$:

$$\sigma = B(J,\zeta) = \frac{2J+1}{2J}\coth\left(\frac{2J+1}{2J}\zeta\right) - \frac{1}{2J}\coth\left(\frac{\zeta}{2J}\right),$$

where ζ represents a ratio of thermal and magnetic energies and J the total angular-momentum quantum number. With T as the absolute temperature and T_N the Néel temperature, the parameter ζ is obtained numerically from the condition valid in the vicinity of T_N:

$$B(J,\zeta) = \frac{T}{T_N}\frac{J+1}{3J}\zeta.$$

The temperature dependence of the integrated intensity of the magnetic reflection 103 for $YBa_2Fe_3O_{7.86}$, as fitted by the least-squares Levenberg–Marquardt method to the scaled square of the Brillouin function, is shown in Fig. 4. The dependence of T_N on the oxygen non-stoichiometry expressed in terms of w shows rather modest variation between some 630 and 670 K. Also in $YBa_2Cu_3O_{6+w'}$, T_N is nearly constant [28] for small w'.

4. Discussion

It seems most convenient to discuss the structural features of $YBa_2Fe_3O_{8+w}$ in relation to the corresponding observations for $YBa_2Cu_3O_{6+w'}$. Obvious differences in oxygen content and T-metal coordination have been discussed previously in Refs. [3,17]. Of more subtle differences it is interesting to compare the bond lengths (for $YBa_2Fe_3O_{8+w}$ in Tables 5 and 6) toward the apical oxygen O(1): The distance Fe(1)–O(1) of the octahedrally coordinated iron is considerably longer than Fe(2)–O(1) of the adjacent Fe(2) square-pyramid (2.17 versus 1.85 Å, for $w_{NPD} = -0.08$). In the cuprate, the square-pyramidal copper has a much longer distance to the apical oxygen than the square-planar copper (2.30

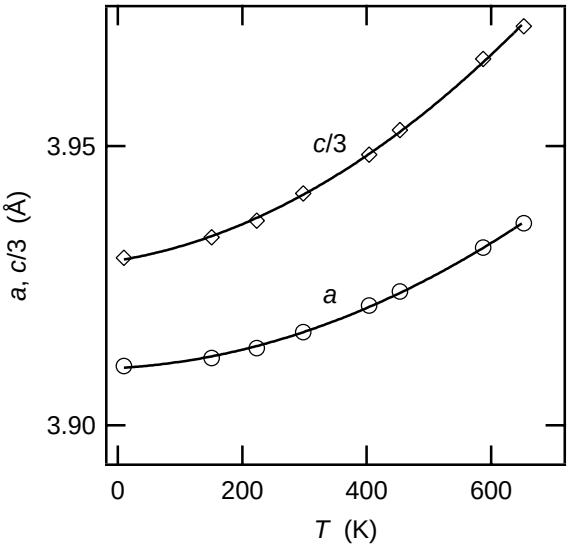

Fig. 3. Temperature variation of unit-cell parameters for tetragonal $YBa_2Fe_3O_{8.08}$.

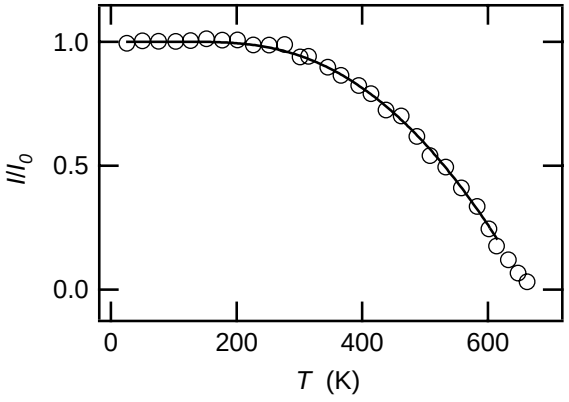

Fig. 4. Brillouin fitting of the temperature variation for the relative intensity of the magnetic reflection 103 (nuclear $\frac{1}{2},\frac{1}{2},\frac{3}{2}$) for $YBa_2Fe_3O_{7.86}$; $T_N = 663(1)$ K.

versus 1.85 Å, for $w'_{NPD} = 0.90$ [26]). Hence in both phases, the T site that has the lower coordination number (CN) attracts the apical O(1) oxygen, which is "free" to move along c in the Ba slab whereas the other oxygen atoms are more or less constrained by the perovskite network. This movement of the apical oxygen demonstrates that both structures, at their integer, stoichiometric compositions $YBa_2Fe_3O_8$ and $YBa_2Cu_3O_7$, tend to equalize the oxidation states of the Cu and Fe atoms between the two types of coordination polyhedra. A bond-valence analysis by Brown [29] has shown that the structure of $YBa_2Cu_3O_7$ relaxes by means of charge transfer between the two crystallographically different Cu atoms that gives to each of them an oxidation state of about 2.33. In case of $YBa_2Fe_3O_8$ it was argued [3] that the equal, experimentally determined, values of the Fe(1) and Fe(2) ordered magnetic moments may suggest that these two atoms have a very similar oxidation state.

Table 5
Selected interatomic distances (Å) in tetragonal $YBa_2Fe_3O_{8+w}$ at 298 K as derived from data in Table 3

	w_{NPD}			
	0.095(3)	0.079(4)	0.059(5)	−0.08(2)
Fe(1)–O(1)	2.154(2)	2.147(2)	2.126(2)	2.170(2)
Fe(1)–O(4,5)	1.9565(1)	1.9658(1)	1.9565(1)	1.9574(1)
Fe(2)–O(1)	1.857(4)	1.866(4)	1.885(4)	1.847(3)
Fe(2)–O(2,3A)	2.0193(6)	2.0184(6)	2.0190(6)	2.0210(4)
Fe(2)–O(2,3B)	1.9565(1)	1.9570(1)	1.9565(1)	
Fe(2)–O(6)	1.893(1)	1.892(1)	1.895(1)	
Ba–O(1)	2.7736(4)	2.7733(4)	2.7719(3)	2.7778(4)
Ba–O(2,3A)	3.212(2)	3.208(3)	3.215(2)	3.240(2)
Ba–O(2,3B)	2.834(4)	2.812(3)	2.836(2)	
Ba–O(4,5)	2.771(2)	2.773(2)	2.769(2)	2.7557(2)
Y–O(2,3A)	2.4019(7)	2.4044(7)	2.4036(7)	2.4005(8)
Y–O(2,3B)	2.721(2)	2.7251(9)	2.7236(9)	
Y–O(6)	2.7670(1)	2.7673(1)	2.7669(1)	
O(2,3B)–O(1)	2.699(3)	2.6844(2)	2.717(2)	
O(2,3B)–O(6)	2.721(2)	2.7614(9)	2.7236(9)	

Table 6
Selected bond distances (Å) in orthorhombic $YBa_2Fe_3O_{8+w}$ at 298 K as derived from data in Table 4

	w_{NPD}	
	−0.16(6)	−0.18(4)
Fe(1)–O(1)	2.147(4)	2.133(2)
Fe(1)–O(4)	1.9611(1)	1.9627(1)
Fe(1)–O(5)	1.9555(1)	1.9537(1)
Fe(2)–O(1)	1.855(4)	1.873(4)
Fe(2)–O(2)	2.022(2)	2.020(1)
Fe(2)–O(3)	2.024(2)	2.021(1)
Ba–O(1)	2.7764(6)	2.7728(3)
Ba–O(2)	3.230(9)	3.198(5)
Ba–O(3)	3.214(9)	3.167(6)
Ba–O(4)	2.762(3)	2.792(2)
Ba–O(5)	2.766(3)	2.798(2)
Y–O(2)	2.397(5)	2.396(2)
Y–O(3)	2.402(5)	2.407(3)

Another manifestation of the charge equalization is that the Fe(2) atom is closer by about 0.2 Å to the center of its square pyramid (which represents the lower-CN polyhedron in the iron-based phase) than Cu(2) is in within the same coordination (which represents the higher-CN polyhedron in the cuprate). The T–T distance across the Y layer is thus some 0.4 Å longer in $YBa_2Fe_3O_8$ than in $YBa_2Cu_3O_7$, while the oxygens [O(2,3) in the iron compound] remain within the same contact range of some 2.85 Å. It is the shortening of this T–T distance that opens the possibility for the contraction in c upon reduction of $YBa_2Fe_3O_8$, despite the inevitable slight increase in the (average) ionic size of iron. In this process, a hypothetical end situation with Fe-coordination squares at both sites would be approached by making the Fe(2)–O(1) interaction

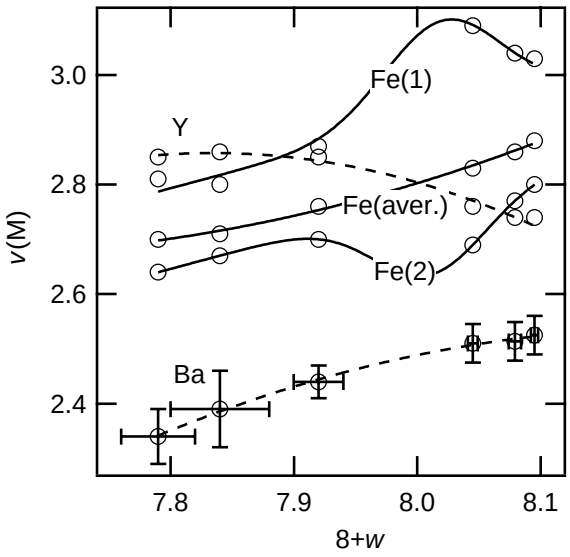

Fig. 5. Bond-valence sums in $YBa_2Fe_3O_{8+w}$ versus oxygen content as obtained from NPD data at 10 K. The curves serve as guides for eye. Typical error bars are indicated for Ba.

insignificant and moving the Fe atoms into the centers of the squares; similar in $YBa_2Cu_3O_7$ (see Fig. 2). In $YBa_2Fe_3O_8$ this would be triggered by removal of O(4) from the Fe(1) octahedron, where upon the thus formed coordination square becomes the lower-CN polyhedron and induces the charge transfer. The experimentally established fact that this square chooses to have its oxygen on the O(5) site that is closer to Fe(1) than is O(4) in the orthorhombically distorted structure proves that Fe(1) competes for a bond strength that cannot be obtained merely by attracting the apical oxygen.

These findings suggest that it could be beneficial to analyze the refined structural data in terms of bond valences [30]. Because the iron valences in nonstoichiometric $YBa_2Fe_3O_{8+w}$ are by definition variable, the actual value of the bond-valence coefficient for iron was computed iteratively from the single-bond lengths for di-, tri-, and tetravalent iron (1.734 [30], 1.759 [30], and 1.78 Å [31], respectively). The calculated bond-valence sums $v(M)$ for the metal atoms (M) in $YBa_2Fe_3O_{8+w}$ are plotted in Fig. 5 against the oxygen content $8+w$. The overall structural compromise appears to be that barium is overbonded whereas yttrium is underbonded throughout the entire nonstoichiometry range. This of course is a consequence of two atoms of unequal size being confined within the perovskite-type framework. Also the average Fe valence in general reflects underbonding, but otherwise complies with the trend in the overall formal oxidation state dictated by the oxygen content. It is interesting to note that the bond valences of barium and yttrium change just as much as the bond valence of the redox element iron. When $w<0$, oxygen vacancies are inserted into the BaO_{12} cuboctahedron (whereas nothing happens to the YO_8 cube) and v(Ba) decreases accordingly. When $w>0$, oxygen atoms are inserted into the coordination sphere of Y (the Ba coordination remains unchanged), yet the Y bond-valence sum decreases whereas v(Ba) continues to increase. The origin of this surprising behavior is the large size of the oxygen atom. The added oxygen O(6) separates the top and bottom of the Y-coordination polyhedron more than it itself contributes in terms of the Y bond-valence sum. In contrast, the relatively small yttrium ion forces a close contact upon O(6) and Fe(2), and the $w>0$ situation therefore increases significantly the Fe(2) bond-valence sum. This is clearly seen in Fig. 5. Upon a hypothetical full occupancy of the O(6) site $(w=1)$, the coordination octahedron of Fe(2) would generate a higher bond-valence sum than the octahedron at Fe(1), because the Fe(1) octahedron is located between eight bulky Ba atoms whereas the Fe(2) octahedron has four smaller Y atoms on one side and four large Ba on the other (Fig. 1). A different situation occurs for the iron atoms upon insertion of oxygen vacancies (for $w<0$). Because this process takes place in the coordination sphere of Fe(1), it decreases straightforwardly v[Fe(1)]. However, the bond-valence sum at Fe(2) is decreased as well, via the valence-equalizing shift of the apical oxygen O(1) toward Fe(1) (*vide supra*), in line with the Pauling's [32] parsimony rule.

Returning to the comparison with $YBa_2Cu_3O_{6+w'}$, we note that the equalizing response to the nonstoichiometry is not found in the cuprate. The difference is that a third, rather stable coordination situation comes into picture when w' is decreased from $w'=1$, viz. the linear O–Cu–O bonding typical of monovalent copper (see Fig. 2). The charge balance under the formation of Cu^{I} maintains Cu(2) above the divalent level throughout most of the homogeneity range. This increases the superconductivity span along w' via the famous mechanism of charge reservoir at Cu(1) and pairing center at Cu(2).

Although more subtle than the effect of nonstoichiometry, also temperature affects the individual bond lengths. The case for the composition $w=0.08$ is illustrated in Fig. 6, which shows that significant variations occur in the apical distances Fe(1)–O(1) and Fe(2)–O(1) as a function of temperature. More specifically, O(1) moves away from Fe(1) toward Fe(2) with increasing temperature. This shift, therefore, may take place to facilitate equalization of the valences of the two iron atoms. A complementary explanation would be that the increased temperature implies an increased effective "compression" of the bond network [six bonds at Fe(1) and five bonds at Fe(2)]. Hence a purely isotropic compression would lead to a net charge transfer of holes to Fe(1), in line with reasoning in Ref. [2]. The mentioned movement of O(1) may be imagined to compensate for this transfer. This could

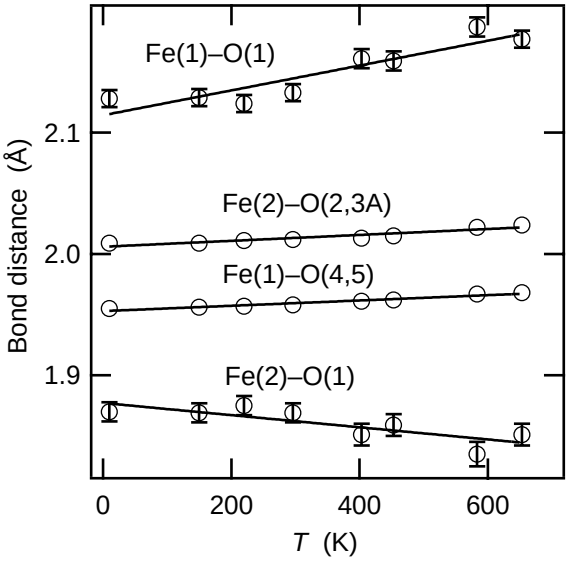

Fig. 6. Temperature variation of selected Fe–O distances for tetragonal $YBa_2Fe_3O_{8.08}$.

also be the reason for the 2.5 times larger expansion along the *c*-axis than in the other two directions.

In conclusion it may be recapitulated that the tetragonal crystal structure of $YBa_2Fe_3O_8$ becomes orthorhombic under insertion of oxygen vacancies into the iron coordination octahedron, in a manner similar to the insertion of additional oxygens to the linear copper coordinations of the tetragonal $YBa_2Cu_3O_6$. Increasing temperature diminishes the orthorhombic distortion due to disordering of the oxygen vacancies aligned along the *b*-axis. The locus of the oxygen defects in the crystal structure of $YBa_2Fe_3O_{8+w}$ represents an interesting Frenkel-type situation; vacancies occur in the Fe(1) octahedron $(w<0)$, whereas the extra oxygens $(w>0)$ are supplementing the Fe(2) square pyramids. Antiferromagnetic ordering of the iron magnetic moments occurs below T_N of 630–670 K, implying that the variation in the oxygen content is too small to significantly affect the magnetic exchange interactions.

References

[1] R.J. Cava, A.W. Hewat, E.A. Hewat, B. Batlogg, M. Marezio, K.M. Rabe, J.J. Krajewski, W.F. Peck, L.W. Rupp, Physica C 165 (1990) 419.
[2] P. Karen, H. Fjellvåg, A. Kjekshus, J. Solid State Chem. 97 (1992) 257.
[3] Q. Huang, P. Karen, V.L. Karen, A. Kjekshus, J.W. Lynn, A.D. Mighell, N. Rosov, A. Santoro, Phys. Rev. B: Condens. Matter 45 (1992) 9611.
[4] I. Morgenstern, Z. Phys. B: Condens. Matter 70 (1988) 299.
[5] Y. Kitaoka, K. Ishida, S. Hiramatsu, K. Asayama, J. Phys. Soc. Jpn. 57 (1988) 734.
[6] A. Aharony, R.J. Birgenau, A. Conigli, M.A. Kastner, H.E. Stanley, Phys. Rev. Lett. 60 (1988) 1330.
[7] M. Cyrot, J.-P. Julien, D. Mayou, Physica C 153–155 (1988) 1257.
[8] A.E. Ruckenstein, P.J. Hirschfeld, J. Appel, Phys. Rev. B: Condens. Matter 36 (1987) 857.
[9] V.J. Emery, G. Reiter, Phys. Rev. B: Condens. Matter 38 (1988) 4547.
[10] M. Kohmoto, J. Friedel, Phys. Rev. B: Condens. Matter 38 (1988) 7054.
[11] Y. Guo, J.-M. Langlois, W.A. Goddard, Science 239 (1988) 896.
[12] S.H. Lee, W.T. Kim, J.D. Jung, Sae Mulli 29 (1989) 614.
[13] Y. Matsumoto, J. Hombo, J. Solid State Chem. 93 (1991) 395.
[14] M. ElMassalami, A. Elzubair, H.M. Ibrahim, M.A. Rizgalla, Physica C 183 (1991) 143.
[15] P. Karen, P.H. Andersen, A. Kjekshus, J. Solid State Chem. 101 (1992) 48.
[16] P. Karen, A. Kjekshus, J. Solid State Chem. 112 (1994) 73.
[17] I.N. Sora, Q. Huang, J.W. Lynn, N. Rosov, P. Karen, A. Kjekshus, V.L. Karen, A.D. Mighell, A. Santoro, Phys. Rev. B: Condens. Matter 49 (1994) 3465.
[18] Y.K. Atanassova, V.G. Hadjiev, P. Karen, A. Kjekshus, Phys. Rev. B: Condens. Matter 50 (1994) 586.
[19] P. Karen, A. Kjekshus, J. Am. Ceram. Soc. 77 (1994) 547.
[20] I. Barin, O. Knacke, Thermochemical Properties of Inorganic Substances, Springer, Berlin, 1973, pp. 316, 584.
[21] I. Barin, O. Knacke, O. Kubashevski, Thermochemical Properties of Inorganic Substances, Supplement, Springer, Berlin, 1977, p. 295.
[22] P.E. Werner, The Computer Programme SCANPI9, Institute of Inorganic Chemistry, University of Stockholm, Sweden, 1992.
[23] J. Fiala, Silikaty 29 (1985) 273.
[24] H.M. Rietveld, J. Appl. Crystallogr. 2 (1969) 65.
[25] A.C. Larson, R.B. Von Dreele, General Structure Analysis System, Los Alamos National Laboratory, Report LAUR 86-748, 1994.
[26] J.D. Jorgensen, B.W. Veal, A.P. Paulikas, L.J. Nowicki, G.W. Crabtree, H. Claus, W.K. Kwok, Phys. Rev. B: Condens. Matter 41 (1990) 1863.
[27] J. Lindén, A. Kjekshus, P. Karen, J. Miettinen, M. Karppinen, J. Solid State Chem. 139 (1998) 168.
[28] C. Vettier, P. Burlet, J. Y. Henry, M. J. Jurgens, G. Lapertot, L. P. Regnault, J. Rossat-Mignod, Phys. Scr. T 29 (1989) 110.
[29] I.D. Brown, J. Solid State Chem. 90 (1991) 155.
[30] I.D. Brown, D. Altermatt, Acta Crystallogr. Sec. B 41 (1985) 244.
[31] N.E. Brese, M. O'Keeffe, Acta Crystallogr. Sec. B 47 (1991) 192.
[32] L. Pauling, J. Am. Chem. Soc. 51 (1929) 1010.